Analysis of viscosity function models used in friction stir welding

Y. C. Silva[1] · F. J. V. Oliveira Júnior[2] · F. Marcondes[2] · C. C. Silva[2]

Abstract

Friction stir welding (FSW) is a solid-state process, where a tool that consists of a shoulder and a pin rotates between the plates to be welded by plastic deformation. This process involves several physical phenomena. To better understand this complex phenomenon, simulations have been performed for a range of maximum viscosity values. The viscosity model used in friction stir welding simulations depends on two variables, the temperature and strain rate; however, the viscosity goes toward infinity for low values of temperature and strain rates. This study analyzed two different friction stir welding simulation, by observing how the viscosity functions behave for low values of temperature and strain rates. The maximum viscosity value was shown to be restricted to values, where the velocity field tends to zero. Furthermore, when the viscosity value exceeds the maximum value, the temperature and viscosity field is significantly impaired. In the correct results, the change in viscosity is restricted to stir zone.

Keywords FSW process · Numerical simulation · Viscosity function model · Fluent simulator · Material flow

1 Introduction

Friction stir welding (FSW) is a solid-state welding system, which was developed by The Welding Institute (TWI, UK) in 1991[1]. This process consists of a tool formed by a shoulder and a pin that rotates between the plates that will be welded by plastic deformation, as shown in Fig. 1. The heat is generated by friction between the rotating tool and the contact surface, as well as by plastic deformation of the material in the vicinity of the joint line. These materials are joined due to the flow of softened material during the passage of the rotating tool between the plates[2].

The FSW process has several advantages over traditional fusion welding processes. For instance, low temperature decreases the residual stress and distortion of the welded material. Another advantage is the possibility of grain refining, because of the reduction in temperature and rotation of the tool minimize the grain size or can cause the refining of the grains by dynamic recrystallization[3].

The FSW method involves several coupled physical phenomena such as welding and rotational speed that influences the welding process. Due to the importance and complexity of this process, various numerical simulations have been developed and analyzed in order to understand the influence of each parameters on the results[4–7].

The early numerical analyses of the FSW processes were based on heat conduction, but these did not take into account the plastic flow near the tool. Frigaard[8] modeled the heat flow in an aluminum alloy. The authors considered that the heat generated was caused by the friction between the tool and workpiece. In their study, the friction coefficient was adjusted at each time step, because the model did not consider the formation of a liquid film between the tool and workpiece for the conditions analyzed.

As these numerical models evolved, the simulations began to consider the flow of material around the tool.

✉ Y. C. Silva
yuri.cruz@ifce.edu.br

F. J. V. Oliveira Júnior
junior180594@alu.ufc.br

F. Marcondes
marcondes@ufc.br

C. C. Silva
cleiton@metalmat.ufc.br

1. Department of Teaching, Crateús Campus, Federal Institute of Education, Science and Technology of Ceará - IFCE, Crateús, CE 63708-260, Brazil

2. Department of Metallurgical and Materials Engineering, Center of Technology, Campus of Pici, Universidade Federal do Ceará - UFC, Fortaleza, CE 60455-760, Brazil
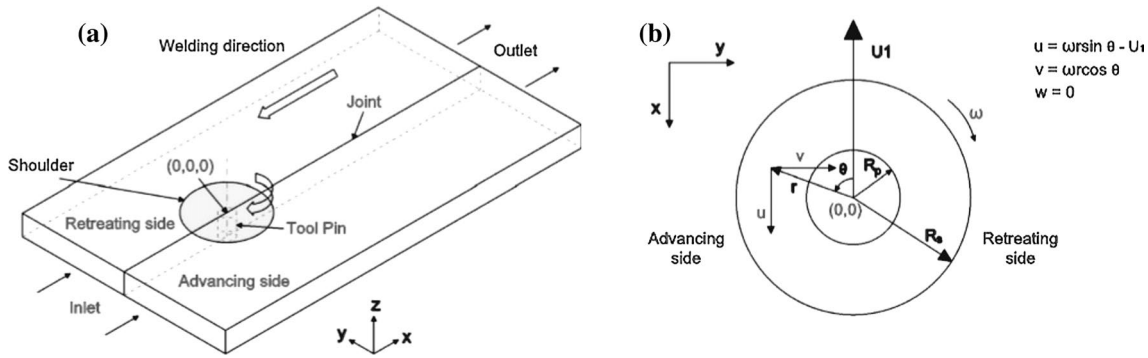
Fig. 1 Schematic diagram used in FSW simulations. **a** The top viewer of tool and **b** velocity boundary conditions

Seidel[9] developed a 2D model based on fluid mechanics, where the viscosity of the material was a function of temperature and strain rate. This viscosity model was proposed by Sellars[10] and later on was modified by Sheppard[11].

Using the viscosity model developed by Sheppard[11], Ulysse[12] developed a 3D model for friction stir welding. Using the same model of Ulysse[12], Nandan[13] also performed a 3D investigation, but now for the AISI 304 stainless steel. In this work, the commercial software FLUENT was used. Nandan also simulated other materials using the same commercial simulator[14, 15].

Despite the large number of papers involving the simulation of the FSW process, a detailed analysis of the behavior of the viscosity functions was not found in these previously mentioned papers. A detailed analysis is important because when low temperatures and low strain rates are applied to the current models used to simulate the FSW, the viscosity approaches the infinity. However, it is well known that the viscosity value is finite. Therefore, due to such behavior, the viscosity function must be truncated. This study analyzed two viscosity models used in FSW simulations with different truncation parameters and the results were shown to be sensitive to the maximum viscosity value used.

2 Mathematical modeling

The FSW process consists of three steps. The first step is the penetration of the tool into the workpiece, the second step is when the tool moves through the workpiece , and third step is the withdrawal of the tool from the workpiece. In this study, two distinct materials, Ti–6Al–4V alloy and AISI 304 alloy, were used and only the second step of the welding process was analyzed.

The analysis of the second part of the welding was chosen because this region represents the main part of the weld. This study analyzed the weld under a steady-state condition, where the tool contact is fixed and the plate is assumed to move as a

continuous fluid flow. It is also assumed that the shoulder was in contact with the top surface of the workpiece, as shown in Fig. 1. In addition, the pin completely penetrated the workpiece. Throughout the welding, the pressure, rotation and welding speed were considered constant, and the shear stress $\tau = \sigma_{\text{yield}}/\sqrt{3}$, where σ_{yield} is evaluated using the distortion energy theory for the plane stress.

The materials were assumed to be non-Newtonian, incompressible and viscoplastic fluids. A partial sticking condition was assumed between the tool and the workpiece and the tilt angle of the tool was taken to be zero[13]. The reference coordinates were fixed in the center of the tool and on the top surface of the workpiece. After a grid refinement study, a non-uniform grid composed of only hexahedrons (1,645,020 nodes and 1,763,904 elements for the AISI stainless steel 304 and 1,645,020 nodes and 1,763,904 elements for the Ti–6Al–4V alloy) was modeled using the ICEM-Mesh Software, and these grids were used for all simulations.

2.1 Governing equations

The continuity equation for an incompressible, single-phase material is given by

$$\frac{\partial u_i}{\partial x_i} = 0; \quad i = 1, \dots, 3 \tag{1}$$

where u is the velocity of the plastic flow at $x - (1)$, $y - (2)$, and $z - (3)$ coordinates. Equation (1) states that the volume variation is null. The momentum conservation equation regarding a co-ordinate system attached to the tool using, the indicial notation again, is given by Cho[2].

$$\frac{\partial \rho u_j}{\partial t} + \frac{\partial \rho u_i u_j}{\partial x_i} = -\frac{\partial P}{\partial x_j} + \frac{\partial}{\partial x_i}\left(\mu \frac{\partial u_j}{\partial x_i}\right) - \rho U \frac{\partial u_j}{\partial x_1} \tag{2}$$

where U is the weld velocity, ρ is the density, P is the pressure, and μ is the non-Newtonian viscosity of the material. Two different models, which will be shown in the

next sub-section, were used for the AISI stainless 304 steel and Ti–6Al–4V alloy. The viscosity model was evaluated through two different models for AISI stainless 304 steel and Ti–6Al–4V alloy. The energy conservation equation is given by

$$\frac{\partial(\rho C_P T)}{\partial t} + \frac{\partial(\rho C_P u_i T)}{\partial x_i} = -\rho C_P U_1 \frac{\partial T}{\partial x_1} + \frac{\partial}{\partial x_i}\left(k\frac{\partial T}{\partial x_i}\right) + S_i + S_b \tag{3}$$

The simulation was performed under a steady-state regime. However, the transient terms are kept in Eqs. (2)–(3) in order to reach the steady-state through a distorted transient. In Eq. (3), C_P is the specific heat and k is the thermal conductivity. S_i and S_b are heat sources that are added to the Fluent simulator in the area of the domain between the tool and workpiece. S_i is a source term that denotes the rate of energy per unit of volume dissipated by friction between tool and workpiece, and S_b denotes the rate of energy per unit of volume generated by plastic deformation in the workpiece away from the interface.

2.2 Viscosity

In this work, two viscosity plasticity models, based on the works of Nandan[13, 15], were investigated for AISI 304 stainless steel and Ti–6Al–4V alloy, respectively. In both models, the viscosity (μ) is given by

$$\mu = \frac{\sigma_e}{3\dot{\epsilon}} \tag{4}$$

However, different equations to evaluate the flow stress (σ_e) were used for each material.

2.2.1 Flow stress for the Ti–6Al–4V alloy

The viscosity model used in the simulation of Ti–6Al–4V alloy was based on the formulation of the flow stress (σ_e) proposed by Sheppard[11], where the flow stress is a function of the effective strain rate ($\dot{\epsilon}$) and temperature (T), which is given by

$$\sigma_e = \frac{1}{\alpha}\sinh^{-1}\left[\left(\frac{Z}{A}\right)^{\frac{1}{n}}\right] \tag{5}$$

where α, A, and n are the material constants and Z is the Zener–Hollomon parameter that is a function of temperature and the effective strain rate, and it is given by

$$Z = \dot{\epsilon}\exp\left(\frac{Q}{RT}\right) \tag{6}$$

In Eq. (6), Q is the temperature-independent activation energy and $\dot{\epsilon}$ is the effective strain rate, which with the assumption of infinitesimal deformation is given by

$$\dot{\epsilon} = \left(\frac{1}{2}\dot{\epsilon}_{ij}\dot{\epsilon}_{ji}\right)^{\frac{1}{2}} \tag{7}$$

$$\dot{\epsilon}_{ij} = \frac{1}{2}\left(\frac{\partial u_i}{\partial x_j} + \frac{\partial u_j}{\partial x_i}\right) \tag{8}$$

The above equations were incorporated into the FLUENT Software using a user definition function (UDF). However, as the UDF does not have the function $\sinh^{-1}$, this function in Eq. (5) was replaced by

$$\sinh^{-1}\left[\left(\frac{Z}{A}\right)^{\frac{1}{n}}\right] = \ln\left\{\left(\frac{Z}{A}\right)^{\frac{1}{n}} + \sqrt{\left[\left(\frac{Z}{A}\right)^{\frac{2}{n}} + 1\right]}\right\} \tag{9}$$

Figure 2 shows the viscosity profiles using the model described above for the Ti–6Al–4V alloy.

2.2.2 AISI 304 stainless steel flow stress

The viscosity model for the AISI 304 stainless steel was based on a simplified Hart's model[16], where the flow stress (σ_e) is calculated with the sum of σ_p (plastic contributions) and σ_v (viscous contributions).

$$\sigma_e = \sigma_p + \sigma_v \tag{10}$$

The plastic contribution is the resistance from the dislocation entanglement and the viscosity contribution represents the frictional force along the slip plane that resists the
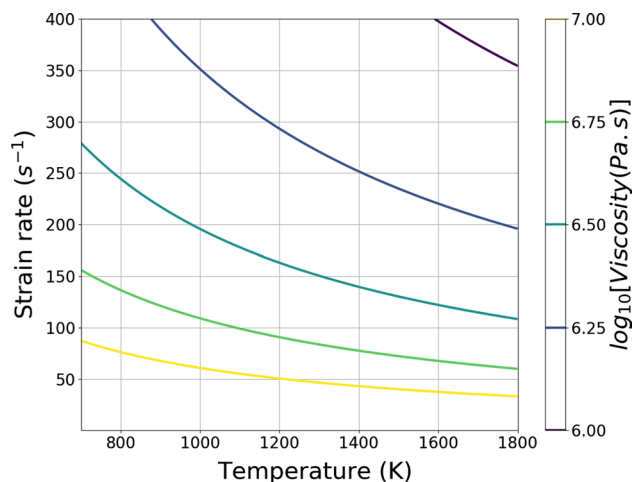

Fig. 2 Logarithm with a base 10 of the viscosity (Pa.s) profiles for the Ti–6Al–4V alloy as a function of temperature and strain rate

dislocation glide. In this model, both contributions depend on temperature and strain rate. The plastic and viscosity contributions to the flow stress are given by

$$\sigma_p = k_1 \exp\left[-\left(\frac{b}{\dot{\epsilon}}\right)^{\lambda}\right] \tag{11}$$

$$b = b_0 \left(\frac{k}{G}\right)^N \exp\left[-\left(\frac{Q}{RT}\right)\right] \tag{12}$$

$$\sigma_v = G\left(\frac{\dot{\epsilon}}{G}\right)^{1/M} \tag{13}$$

$$a = a_0 \exp\left[-\left(\frac{Q^0}{RT}\right)\right] \tag{14}$$

where T is the absolute temperature (K) and R is the universal gas constant. The other constants are material parameters, and they are determined from experiments. These parameters were determined by Cho[17], who developed a study about the modeling strain hardening and texture evolution of the 304 stainless steel in FSW.

The k_1 parameter is the maximum value of the viscosity contribution to the stress flow. The saturation value of k_1 depends on the temperature and strain rate, wherein Hart's model is replaced by one with a Voce-like saturation limited state variable and k_1 can be calculated using Eqs. (15) and (16).

$$k_1 = \left(\frac{C}{\varphi}\right)^{m_0} \tag{15}$$

where the Fisher factor is given by Fisher[18] as

$$\varphi = T \dot{\ln}\left(\frac{D_0}{\dot{\epsilon}}\right) \tag{16}$$

Figure 3 shows the viscosity profiles as a function of the strain rate and temperature using the above described model.

2.3 Heat source models for the Ti–6Al–4V alloy and 304 stainless steel

The heat source was also added to the commercial software Fluent by means of UDF (user definition functions). The S_i source term is defined by

$$S_i = q_1 \frac{A_r}{V} \tag{17}$$

where A_r is the contact area between the tool and workpiece and V is the volume enclosing the area A_r. $q_1 [W/m^2]$ is the heat generated by the contact surface between the shoulder tool and workpiece. In this work (q_1) is evaluated by
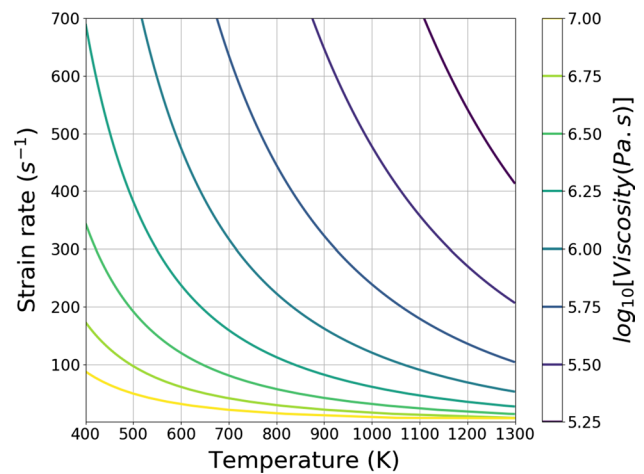

Fig. 3 Logarithm with a base 10 of the viscosity (Pa.s) profiles for the 304 stainless steel as a function of temperature and strain rate

the following expressions for the 304 stainless steel and Ti–6Al–4V alloy, respectively[15, 19]:

$$q_1 = \left[\delta n\tau + (1-\delta)\mu_f P\right](\omega r - U_1 \sin\theta) \tag{18}$$

$$q_1 = \left[(1-\delta)\eta\tau + \delta\mu_f P\right](\omega r - U_1 \sin\theta) \tag{19}$$

In the above equations, P is the pressure of the tool during the welding, ω is the angular velocity, U_1 is the welding speed, η is the thermal efficient, δ is a constant that will be defined later, μ_f is a friction coefficient, the term composed of $(\omega r - U_1 \sin\theta)$ represents the relative velocity between the tool and workpiece, and $\sin\theta$ is defined by

$$\sin\theta = \frac{y}{r} \tag{20}$$

$$\cos\theta = -\frac{x}{r} \tag{21}$$

$$r = \sqrt{x^2 + y^2} \tag{22}$$

where r is the radius and the global axis is fixed in the center of the tool.

Equations (18) and (19) represent the same physical phenomenon, the difference between them is only the way they are written. In the first study performed by Nandan[13], the equation for 304 stainless steel was written in terms of $(1-\delta)$ and the second study also analyzed by Nandan[15], the equation for the Ti–6Al–4V alloy was written in terms of δ. These terms determine the quantity of the heat that will be generated by friction or deformation. This small difference between the equations was not modified in the present investigation, in order to maintain agreement with the previous

works. For AISI stainless steel 304, δ was kept constant and equal to 0.7, while for the Ti–6Al–4V alloy we used the model defined in Deng[20] that is given by

$$\delta = 1 - \exp\left(-\delta_0 \frac{\omega}{\omega_0} \frac{r}{R_s}\right) \tag{23}$$

where R_s is the radius of the shoulder, δ_0 is a constant, and ω_0 is a dimensionless constant for the rotational speed, ω. The friction coefficient (μ_f) was kept constant and equal to 0.4 for the stainless steel and the following expression given in Kong[21] was used for the Ti–6Al–4V alloy:

$$\mu_f = \mu_0 \exp\left(-\delta_0 \frac{\omega}{\omega_0} \frac{r}{R_s}\right) \tag{24}$$

In Eq. (3), $S_b [W/m^3]$ is a heat source term generated by the plastic deformation in the contact of the workpiece and the tool. Alike the S_i term, the UDF from Fluent software was used to implement S_b in W/m^3 from the above equations. This source term has been calculated as $f_m \mu \Phi$, where μ is the viscosity, f_m is an arbitrary constant that indicates the extent of atomic mixing in the system. In this study, a value of 0.04 was used for f_m and Φ[2] is given by

$$\Phi = 2\left(\left(\frac{\partial u_1}{\partial x_1}\right)^2 + \left(\frac{\partial u_2}{\partial x_2}\right)^2 + \left(\frac{\partial u_3}{\partial x_3}\right)^2\right) + \left(\frac{\partial u_1}{\partial x_2} + \frac{\partial u_2}{\partial x_1}\right)^2$$
$$+ \left(\frac{\partial u_1}{\partial x_3} + \frac{\partial u_3}{\partial x_1}\right)^2 + \left(\frac{\partial u_3}{\partial x_2} + \frac{\partial u_2}{\partial x_3}\right)^2 \tag{25}$$

The heat generated by plastic deformation and friction between the contact of the tool and workpiece are split between them. The fraction that is inputted to the plate (f) is defined by Nandan[15] as

$$f = \frac{J_w}{J_t + J_w} \tag{26}$$

where J_w (workpiece) and J_t (tool) are defined by the following equation:

$$J_i = \sqrt{(\rho C_p k)_i}; i = w \text{ or } t \tag{27}$$

A convection boundary condition was also established on all faces of the plate. For the top of the plate, the loss of heat through radiation was added to the convection. Once these conditions are established, the boundary conditions for the bottom, side and top of the plate are, respectively, given by the following equations:

$$k\frac{\partial T}{\partial z} = h_b(T - T_a) \tag{28}$$

$$\pm k\frac{\partial T}{\partial y} = h_s(T - T_a) \tag{29}$$

$$-k\frac{\partial T}{\partial z} = h_t(T - T_a) + \sigma\epsilon(T^4 - T_a^4) \tag{30}$$

where h_b, h_s, and h_t are the heat convection coefficients for bottom, side and top of the workpiece, respectively, T_a is the environment temperature, and k is the thermal conductivity of the workpiece.

At the boundaries, the velocities in the contact regions between the tool and workpiece were set. For the shoulder, the velocity components are given by

$$v_x = (1 - \delta)(\omega r \sin \theta - U_1) \tag{31}$$

$$v_y = (1 - \delta)(\omega r \cos \theta) \tag{32}$$

The velocity of the contact between the tool pin and workpiece is defined by

$$v_x = (1 - \delta)(\omega R_p \sin \theta - U_1) \tag{33}$$

$$v_y = (1 - \delta)(\omega R_p \cos \theta) \tag{34}$$

where R_p is the radius of the pin. All velocity components were implemented in the Fluent simulator using the UDF. All experimental parameters such as size of the workpiece, thermal conductivity, welding speed are presented in "Appendix".

3 Results and discussion

In this study, a hexahedral mesh for the simulations of both materials was used. Mesh refinement tests were performed on the geometry used to simulate the AISI 304 stainless steel and the titanium alloy before the tests with different viscosity truncation values. One example of the mesh used in these simulations is shown in Fig. 4. These meshes have a radial growth because this format allows the region, where the tool is located to have the smallest elements with the rest of the domain having elements of the same size. This mesh model has been observed in other studies[22]. This format of grid was chosen in order to capture the sharp thermal gradients around the workpiece more effectively.

All meshes are constructed as shown in Fig. 4, changing only the number of elements and keeping the dimensions of the workpiece. Three different meshes were tested for both materials. The titanium alloy simulations were performed using meshes with the following number of elements: 1,038,058, 2,875,307, and 4,467,071.
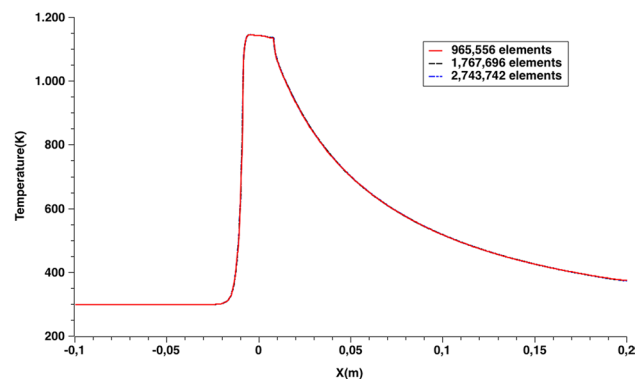
Fig. 4 Example of a mesh used in the simulations
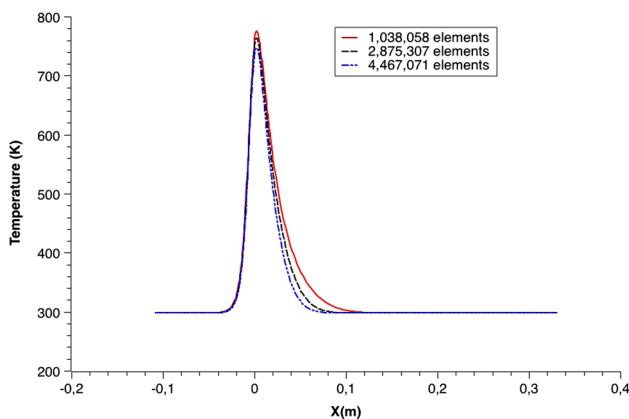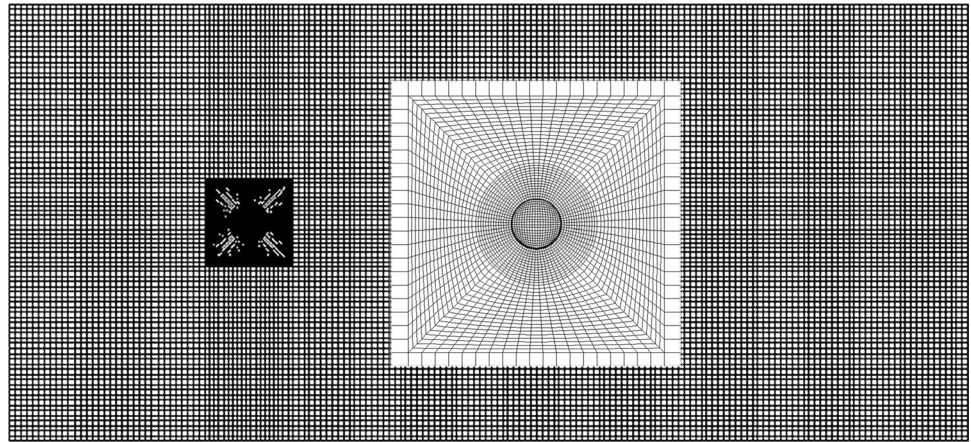
Fig. 5 Mesh refinement study for Ti–6Al–4V

Fig. 6 Mesh refinement study for AISI 304 stainless steel

Figure 5 presents the temperature profile for the titanium alloy along the length of the plate and located 3.17 mm from the center of the tool using the three grids. From this figure, it is possible to observe that the temperature profiles do not change much when the number of elements of the grid are increased. There were some minor differences in the temperature peak and a faster cooling of the plate, when the mesh was refined. However, the differences observed in the cooling stage of the welding cycle did not change the phase properties of the workpiece, since the differences as shown in 5 were verified for temperatures close to the ambient temperature. To be conservative, the mesh with 2,875,307 elements was chosen for the investigation of the titanium alloy.

A similar refinement mesh study was carried out for the AISI 304 stainless steel using the same geometry. Once again, three meshes were used, but now the following number of elements were tested: 965,556, 1,767,696, and 2,743,742. The temperature profile at the position already presented for the titanium alloy is shown in Fig. 6. From this figure, it can be observed that any major variation was observed with all the used grids. However, in order to be conservative for the investigation of the maximum valor

of the viscosity performed in this section, the mesh with 1,767,696 elements was chosen. Herein, just to demonstrate that the chosen grid is enough refined, it is important to mention the three-dimensional numerical investigation for the 409 stainless steel performed by Cho[2] using a mesh composed of 356,862 hexahedral elements for a geometry greater than the one investigated in this work.

After the mesh refinement study, the simulation results were compared with the ones presented for the AISI 304 stainless steel[13] and Ti–6Al–4V alloy[15]. Figures 7 and 8 present the temperature profile for the AISI 304 stainless steel and Ti–6Al–4V alloy, respectively. Based on these figures, although minor differences were observed, we can verify a good agreement between our results and the ones from Nandan[13] and Nandan[15]. Furthermore, no grid refinement study was presented in the above cited works. Finally, the minor difference between the simulated results for both materials did not exceed three percent (3%).

Having performed the grid refinement study and validated the simulations with the numerical results from the literature, it is now investigated the maximum physical value that can be set for the viscosity of the two materials under analysis. Although the maximum viscosity is finite for both
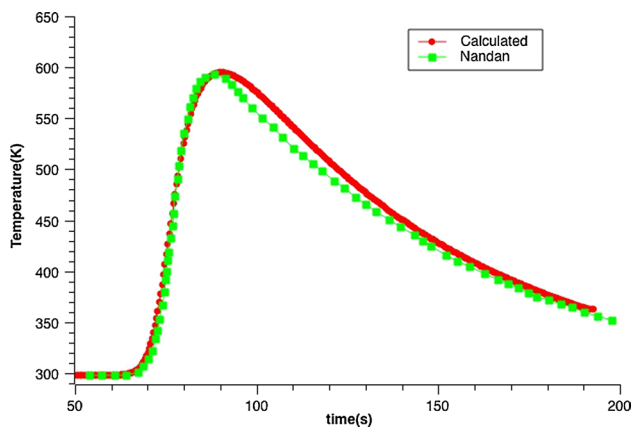
Fig. 7 Comparison of the temperature profiles for the AISI 304 stainless steel. Data evaluated at $y = 18$ mm on the retreating side on the top of the workpiece
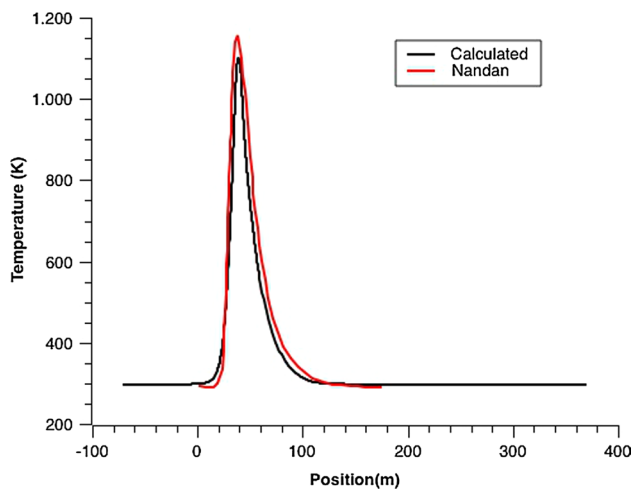
Fig. 8 Comparison of temperature profiles for the Ti–6Al–4V alloy. Data evaluated at $y = 3.17$ mm on the advancing side on the bottom surface of the workpiece

Table 1 Maximum value for the viscosity of each material investigated

Material	Truncation
AISI stainless steel 304	10^7 Pa.s
	10^8 Pa.s
	10^9 Pa.s
Ti–6Al–4V alloy	10^7 Pa.s
	10^8 Pa.s
	10^9 Pa.s

investigated materials, the numerical models proposed in the literature result in infinity values when low values of temperature and strain rate are achieved.

Three possible truncation values, shown in Table 1 for both materials, were tested in this study.

Figure 9 presents the temperature field for both materials using the three maximum values of viscosity presented in Table 1. The effect of increasing the viscosity is to elongate the temperature field in the axial direction, especially for the AISI 304 stainless steel. It is also noted that the maximum temperature decreases when the maximum viscosity increases. The maximum viscosity value that results in the closest expected temperature field to the ones presented in the literature was equal to 10^7 Pa.s. However, in

the literature, there is no mention to the maximum viscosity value used[2, 14, 15]. Finally, it is important to stress that the expected temperature fields are the ones shown in Fig. 9a, b for both materials.

To shed some light on the temperature field behavior, it is presented in Fig. 10 the viscosity field of each material for the three maximum values of viscosity investigated. From this figure, it is possible to observe that the region where the viscosity field changes also increase away from the tool, especially for the 304 stainless steel. This behavior is justified because the 304 stainless steel is more ductile than the Ti–6Al–4V, and therefore the variation in viscosity has a greater impact on the temperature field and vice versa. Finally, if a maximum viscosity equals to 10^7 Pa.s is selected, for both materials, the temperature field is in good agreement with the previous results from the literature as it is shown in Fig. 9. Also, when the maximum viscosity equal to 10^7 Pa.s is chosen, it is possible to verify that that the viscosity field, for both materials, changes only in the region of the tool, which is the region where the material deformation is expected.

In FSW, the thermo-mechanically affected zone does not propagate to regions far from the tool. The results of Yaduwanshi[23] show that the weld zone has approximately the same size as the shoulder.

Aiming to investigate the effect of the maximum value of viscosity in the velocity field, the viscosity and velocity profiles (Fig. 11) are plotted along the welding direction and close to the pin. We choose this line because it is possible to observe the behavior of the two proprieties behind and in front of the tool. Figure 11 shows that when the viscosity reaches values close to 10^7 Pa.s the velocity tends to zero. These values are in agreement with the results described by Nandan[13] using AISI 304 stainless steel and Nandan[15] Ti–6Al–4V alloy. According to the work of Nandan[13] using 304 stainless steel, there is no significant flow of material for viscosities larger than $4 \cdot 10^6$ Pa.s. For titanium alloy, the work performed by Nandan[15] demonstrated that the flow of the material is negligible for viscosities greater than 10^7 Pa.s.

Fig. 9 Temperature field for different maximum values of viscosity. **a**, **b** 10^7 Pa.s. **c**, **d** 10^8 Pa.s. **e**, **f** 10^9 Pa.s
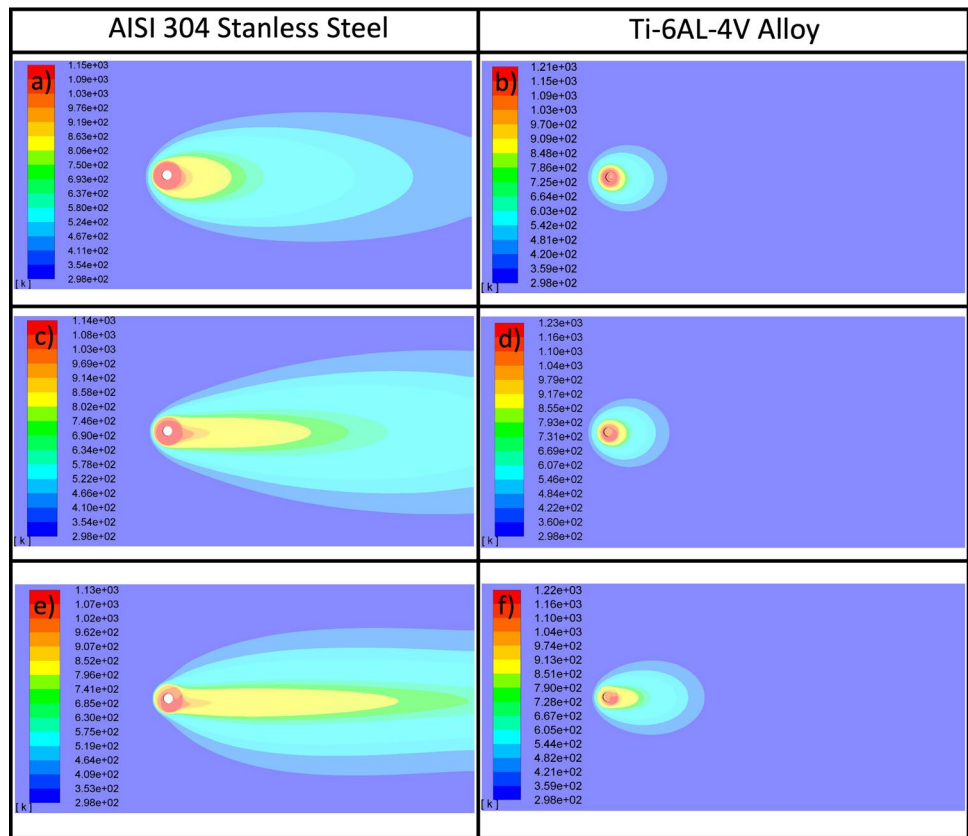
Fig. 10 Viscosity field for different maximum values of viscosity. **a**, **b** 10^7 Pa.s. **c**, **d** 10^8 Pa.s. **e**, **f** 10^9 Pa.s
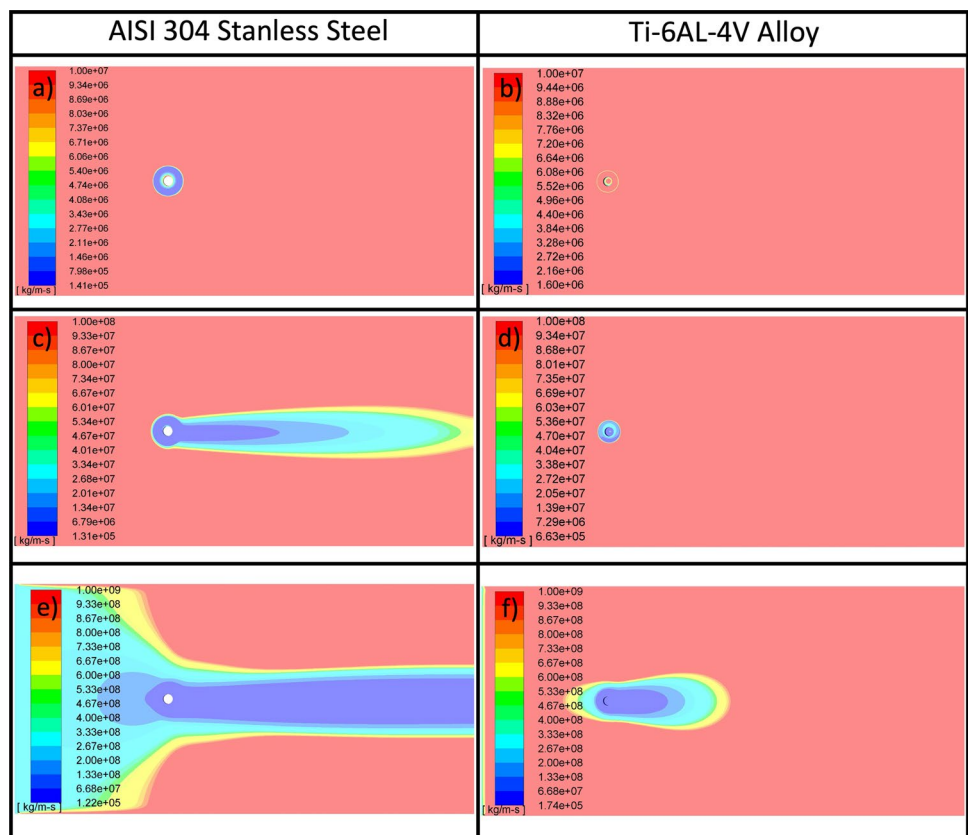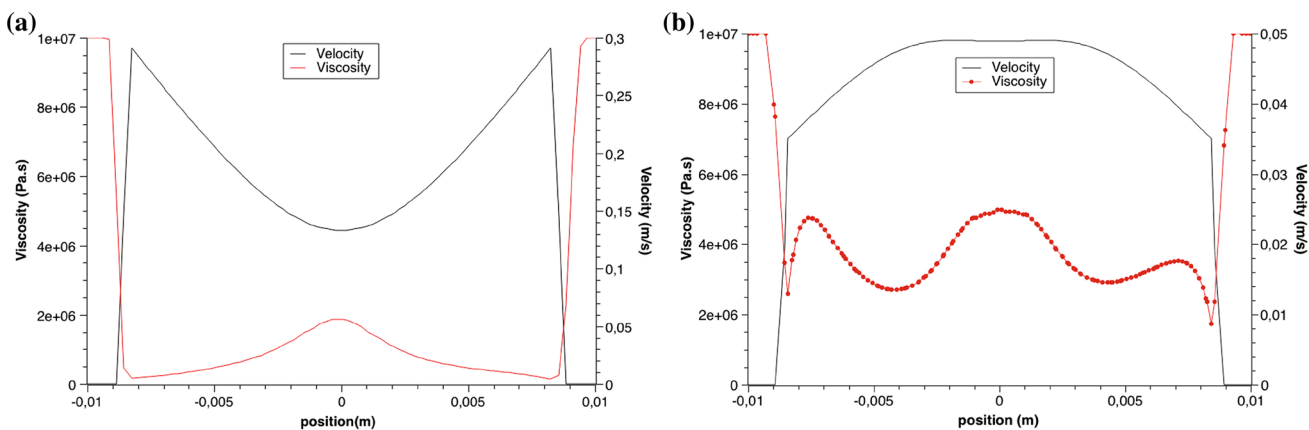
Fig. 11 Velocity and viscosity profiles as a function of position-maximum value of viscosity equal to 10^7 Pa.s **a** AISI 304 stainless steel simulations **b** Ti–6Al–4V alloy simulations
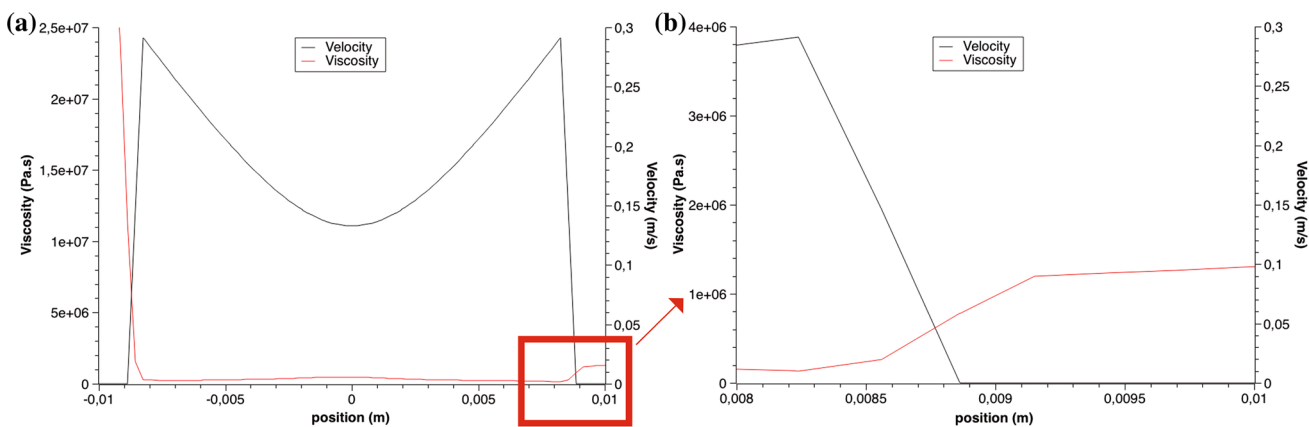

Fig. 12 Velocity and viscosity profiles as a function of the position-maximum value of viscosity equal to 10^9 Pa.s for the AISI 304 stainless steel
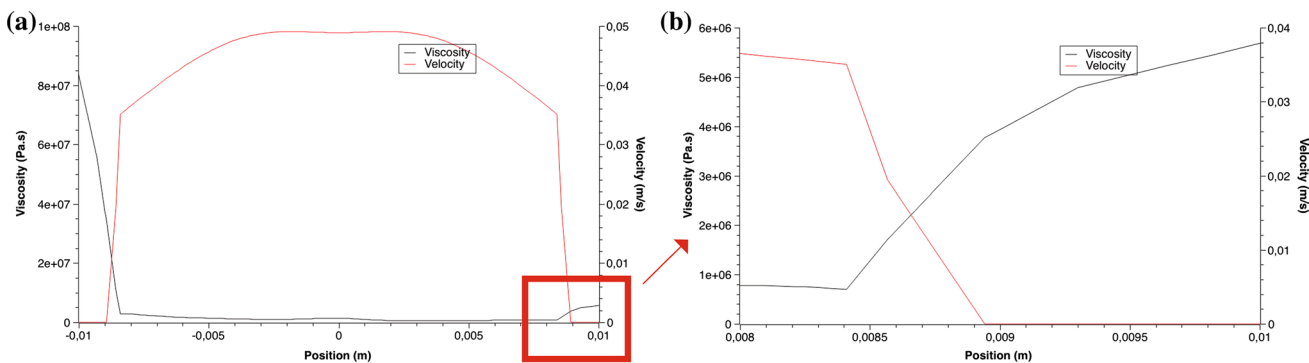

Fig. 13 Velocity and viscosity profiles as a function of the position-maximum value of viscosity equal to 10^9 Pa.s for the Ti–6Al–4V alloy

In order to verify that the velocity always reaches zero for values close to those shown in Fig. 11, the same graph shown in Fig. 11 was built using the highest maximum viscosity value investigated in this work (10^7 Pa.s). Figures 12 and 13 are the graphs for AISI 304 stainless steel and Ti–6Al–4V alloy, respectively. Enlarged figures on the right provide more details of the velocity profiles. These figures show that the viscosity profile presents large values in the region behind the tool, although the velocity profile is null. Once again, the velocity profile becomes null for

viscosity values close to the ones presented in Fig. 11. From Fig. 12, for the AISI 304 stainless steel the maximum value of viscosity, where there is material flow, is approximately 1×10^6 Pa.s, and from Fig. 13, for Ti–6Al–4V alloy, the maximum value of viscosity, where there is material flow, is approximately 2.5×10^6 Pa.s. The material flow ceases for high viscosity values but the viscosity still changes even though the material flow has ceased, for both materials.

As the maximum viscosity value does not affect the range of where the velocity becomes null, we decided to verify the behavior of the velocity field around the shoulder for both materials; the velocity field in this region is shown in Fig. 14 at the top of the workpiece and next to the shoulder. As we can see from Fig. 14, when the maximum value of viscosity is increased there is a region behind the tool that has a velocity different from zero. Therefore, the reason the temperature field presents an elongated shape, see Fig. 9c–f, is due to the advected energy carried out by this non-null velocity region. As the material remains in solid state, there is no physical reason to have non-null velocity regions farther away from the tool, as shown in Fig. 14b, d, for both materials.

4 Conclusions

In this work, the simulation of the friction stir welding (FSW) process of two different materials was investigated. One key parameter in FSW is the maximum viscosity of the material to be used in the simulation for small values of temperature and strain rates of the welded material. In theory, this value goes toward infinity for small values of temperature and strain rate. Herein, we demonstrated using several values of maximum viscosity the point where the viscosity function needs to be truncated and the physical reasons for that truncation. The numerical experiments showed that the temperature and velocity fields depend on the maximum value of the viscosity of the material used, and the maximum value needs to be truncated when the velocity field tends to be null. If we allow the viscosity to be larger than this maximum value, the temperature field will become elongated in the axial direction of the welding due to an increase in the velocity field near the tool.
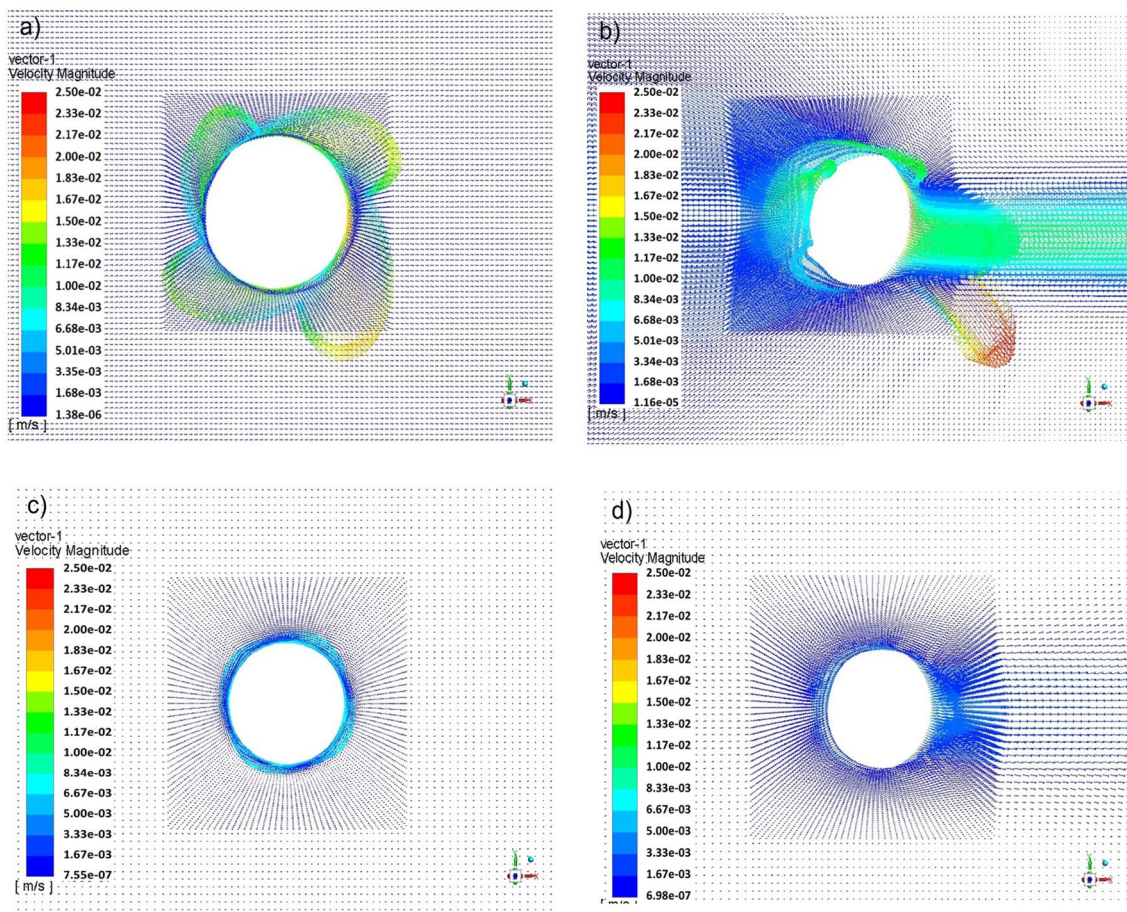
Fig. 14 Velocity field at the top of the workpiece. **a** 10^7 Pa.s, **b** 10^9 Pa.s for 304 steel and **c** 10^7 Pa.s and 10^9 Pa.s for titanium alloy

Appendix

1 AISI 304 stainless steel constants

$C_{\mathrm{P}-workpiece}$ (J/kg K)	$276 + 0.851 \cdot T - 0.000851 \cdot T^2 + 3 \times 10^{-7} \cdot T^3$
$k_{\mathrm{workpiece}}$ (W/m K)	$14.3 - 0.00902 \cdot T + 4.52 \times 10^{-5} \cdot T^2 - 2.49 \times 10^{-8} \cdot T^3$
$\rho_{\mathrm{workpiece}}$ (kg/m^3)	7200
P_N (MPa)	109
R_{s} (mm)	9.53
R_{p} (mm)	3.17
U_1 (mm/s)	1.693
$C_{\mathrm{P}-tool}$ (J/kg K)	$158 + 1.06 \cdot T - 1.63 \cdot T^2$
η	0.5
k_{tool} (W/m K)	$0.367 - 2.29 \cdot T + 1.25 \times 10^{-7} \cdot T^2$
ρ_{tool} (kg/m^3)	19400
δ	0.7
μ	0.4
ω (RPM)	300
a_0 (s^{-1})	1.36×10^{35}
b_0 (s^{-1})	8.03×10^{26}
G (Pa)	73.1×10^9
k_0 (Pa)	150×10^6
Q (J/mol)	410×10^3
Q_0 (J/mol)	91×10^3
λ	0.15
M	7.8
N	5
C (Pa)	132×10^6
D_0 (s^{-1})	10^8
m_0	2.148
n_0	6
R (J/mol K)	8.3144621

2 Ti–6Al–4V alloy constants

$C_{\text{P}-workpiece}$ (J/$kg\,K$)	$622 - 0.367 \cdot T - 0.000545 \cdot T^2 + 2.39 \times 10^{-8} \cdot T^3$
$k_{\text{workpiece}}$ (W/$m\,K$)	$19.2 + 0.0189 \cdot T - 1.53 \times 10^{-5} \cdot T^2 + 1.41 \times 10^{-8} \cdot T^3$
$\rho_{\text{workpiece}}$ (kg/m^3)	7200
θ (MPa)	$9.09 \times 10^2 + 1.11 \cdot T - 3.05 \times 10^{-3} \cdot T^2 + 1.26 \times 10^{-6} \cdot T^3$
P_N (MPa)	60.0
R_{s} (mm)	9.5
R_{p} (mm)	3.95
U_1 (mm/s)	1.6
$C_{\text{P}-tool}$ (J/$kg\,K$)	$128.3 - 3.279 \times 10^{-2} \cdot T + 3.41 \times 10^{-6} \cdot T^2$
k_{tool} (W/$m\,K$)	$153.5 - 9.56 \times 10^{-2} \cdot T + 5.23 \times 10^{-5} \cdot T^2$
ρ_{tool} (kg/m^3)	19400
δ_0	0.7
μ_0	0.4
η	0.7
ω (RPM)	275
A (s^{-1})	229.725
α (MPa^{-1})	0.0066
Q (J/mol)	501000
n	5
P	0.08

References

1. Thomas WMW, Norris I, Nicholas ED, Needham JC, Murch MG, Temple-Smith P, Dawes CJ (1991) Friction stir welding process developments and variant techniques, Intl. Patent Application no PCT/GB92/02203 and GB Patent Application no. 9125978.9

2. Cho HH, Hong ST, Roh JH, Choi HS, Kang SH, Steel RJ, Han HN (2013) Three-dimensional numerical and experimental investigation on friction stir welding processes of ferritic stainless steel. Acta Mater 61(7):2649. https://doi.org/10.1016/j.actamat.2013.01.045

3. Andrade TC, Silva CC, de Miranda HC, Motta MF, Farias JP, Bergman LA, dos Santos JF (2015) Microestrutura de uma solda dissimilar entre o aço inoxidável ferrítico AISI 410S e o aço inoxidável austenítico AISI 304L soldado pelo processo FSW. Soldagem e Inspecao 20(4):467. https://doi.org/10.1590/0104-9224/SI2004.13

4. Al-araji NM, Kadum KM, Al-dayni AA (2011) Effect of friction stir welding pressure on the microstructure and mechanical properties of weld joints. Int J Sci Eng Res 2(12):1

5. Patel N, Bhatt K, Mehta V (2016) Influence of tool pin profile and welding parameter on tensile strength of magnesium alloy AZ91 during FSW. Procedia Technol 23:558. https://doi.org/10.1016/j.protcy.2016.03.063

6. Gadakh VS, Kumar A (2017) FSW tool design using TRIZ and parameter optimization using Grey Relational Analysis. Mater Today Proc 5(2):6655. https://doi.org/10.1016/j.matpr.2017.11.322

7. He X, Gu F, Ball A (2014) A review of numerical analysis of friction stir welding. Prog Mater Sci 65:1. https://doi.org/10.1016/j.pmatsci.2014.03.003

8. Frigaard Ø, Grong Ø, Midling OT (2001) A process model for friction stir welding of age hardening aluminum alloys. Metall Mater Trans A 32(5):1189. https://doi.org/10.1007/s11661-001-0128-4

9. Seidel TU, Reynolds AP (2003) Two-dimensional friction stir welding process model based on fluid mechanics. Sci Technol Weld Join 8(3):175. https://doi.org/10.1179/136217103225010952

10. Sellars CM, Tegart WJM (1972) Hot workability. Int Metall Rev 17(1):1. https://doi.org/10.1179/imtlr.1972.17.1.1

11. Sheppard T, Wright DS (1979) Determination of flow stress: part 1 constitutive equation for aluminum alloys at elevated temperatures. Met Technol. https://doi.org/10.1179/030716979803276264

12. Ulysse P (2002) Three-dimensional modeling of the friction stir-welding process. Int J Mach Tools Manuf. https://doi.org/10.1016/S0890-6955(02)00114-1

13. Nandan R, Roy GG, Debroy T (2006) Numerical simulation of three-dimensional heat transfer and plastic flow during friction stir welding. Metall Mater Trans 37A(4):1247. https://doi.org/10.1007/s11661-006-1076-9

14. Nandan R, Roy GG, Lienert TJ, Debroy T (2007) Three-dimensional heat and material flow during friction stir welding of mild steel. Acta Mater 55(3):883. https://doi.org/10.1016/j.actamat.2006.09.009

15. Nandan R, Lienert TJ, DebRoy T (2008) Toward reliable calculations of heat and plastic flow during friction stir welding of Ti–6Al–4V alloy. Int J Mater Res 99(4):434. https://doi.org/10.3139/146.101655

16. Hart EW (1976) Constitutive relations for the nonelastic deformation of metals. J Eng Mater Technol 98(3):193. https://doi.org/10.1115/1.3443368

17. Cho JH, Boyce DE, Dawson PR (2005) Modeling strain hardening and texture evolution in friction stir welding of stainless steel. Mater Sci Eng A 398(1–2):146. https://doi.org/10.1016/j.msea.2005.03.002

18. Fisher ES (1966) Temperature dependence of the elastic moduli in alpha uranium single crystals, part IV (298 to 923 K). J Nucl Mater 18(1):39. https://doi.org/10.1016/0022-3115(66)90094-8

19. Nandan R, Roy GG, Lienert TJ, DebRoy T (2006) Numerical modelling of 3D plastic flow and heat transfer during friction stir

welding of stainless steel. Sci Technol Weld Join 11(5):526. https://doi.org/10.1179/174329306X107692
20. Deng Z, Lovell MR, Tagavi KA (2001) Influence of material properties and forming velocity on the interfacial slip characteristics of cross wedge rolling. J Manuf Sci Eng 123(4):647. https://doi.org/10.1115/1.1383028
21. Kong HS, Ashby MF (1991) Friction-heating maps and their applications. MRS Bull 16(10):41. https://doi.org/10.1557/S0883769400055822
22. Zhang S, Chen G, Liu Q, Li H, Zhang G, Wang G, Shi Q (2018) Numerical analysis and analytical modeling of the spatial distribution of heat flux during friction stir welding. J Manuf Proces 33:245. https://doi.org/10.1016/j.jmapro.2018.05.021
23. Yaduwanshi DK, Bag S, Pal S (2016) Numerical modeling and experimental investigation on plasma-assisted hybrid friction stir welding of dissimilar materials. Mater Des 92:166. https://doi.org/10.1016/j.matdes.2015.12.039

Publisher's Note Springer Nature remains neutral with regard to jurisdictional claims in published maps and institutional affiliations.

Springer